Applied Physics Letters

RESEARCH ARTICLE | MAY 15 2023

A Lamb wave magnetoelectric antenna design for implantable devices

Ruoda Zheng ; Victor Estrada ; Nishanth Virushabadoss; Alexandria Will-Cole ; Adrian Acosta ; Jinzhao Hu ; Wenzhong Yan ; Jane P. Chang ; Nian X. Sun; Rashaunda Henderson ; Gregory P. Carman ; Abdon E. Sepulveda

Appl. Phys. Lett. 122, 202901 (2023)
https://doi.org/10.1063/5.0151937

Applied Physics Letters ARTICLE pubs.aip.org/aip/apl

A Lamb wave magnetoelectric antenna design for implantable devices

Cite as: Appl. Phys. Lett. **122**, 202901 (2023); doi: 10.1063/5.0151937
Submitted: 26 March 2023 · Accepted: 26 April 2023 ·
Published Online: 15 May 2023

View Online Export Citation CrossMark

Ruoda Zheng,[1,a] Victor Estrada,[1,a] Nishanth Virushabadoss,[2] Alexandria Will-Cole,[3] Adrian Acosta,[4] Jinzhao Hu,[1] Wenzhong Yan,[1] Jane P. Chang,[4] Nian X. Sun,[3] Rashaunda Henderson,[2] Gregory P. Carman,[1] and Abdon E. Sepulveda[1]

AFFILIATIONS

[1]Department of Mechanical and Aerospace Engineering, University of California, Los Angeles, California 90095, USA
[2]Department of Electrical and Computer Engineering, University of Texas at Dallas, Richardson, Texas 75080, USA
[3]Department of Electrical and Computer Engineering, Northeastern University, Boston, Massachusetts 02115, USA
[4]Department of Chemical and Biomolecular Engineering, University of California, Los Angeles, California 90095, USA

[a)]Authors to whom correspondence should be addressed: ruodaz@g.ucla.edu and estradavictor@g.ucla.edu

ABSTRACT

A 400 MHz magnetoelectric (ME) Lamb wave antenna design to function in the medical implant communication service band is proposed. The antenna employs a heterostructure of piezoelectric and magnetostrictive membranes to acoustically excite standing shear bulk wave and radiate as a magnetic dipole. Multiphysics finite element analysis simulations are performed for transmission and reception modes. In these simulations, three aspects are investigated: piezoelectricity, micromagnetic precession, and magnetic dipole radiation. An experimental demonstration of the antenna is also conducted and shows mechanical resonance with a Q-factor of 500 and ME coupling. These results indicate that the design can be operated in zero-order antisymmetric (A_0) mode as a tunable oscillator or sensor. This ME approach provides a solution to the miniaturization problem of traditional current-based implantable antennas.

In recent years, the field of implantable medical devices has seen a trend toward the development of compact antennas that operate at a frequency around 400 MHz for real-time communication through tissue. Conventional antennas rely on electromagnetic resonance, which limits their size to the free space wavelength of the signal they are intended to transmit. To address this limitation, electrically small antennas (ESAs) smaller than $\lambda/10$ have been proposed as a solution for reducing the size.[1–3] However, ESAs still face challenges, such as sensitivity to ground plane effects and decreased radiation efficiency, particularly in electrically lossy environments, such as the human body.[4] To overcome these challenges, magnetoelectric (ME) antennas have been proposed.[5–10]

ME antennas employs a piezoelectric layer to achieve acoustic resonance and a magnetostrictive layer to radiate as a magnetic dipole. The smaller wavelength of acoustic resonance[11–13] allows for easier miniaturization, while the magnetic dipole provides lower signal decay rate in electrically lossy media compared to electric dipoles. Several studies have demonstrated the ability of ME antennas to create significant magnetization changes in small form factors and outperform electric antennas.[14–23]

The initial stage for designing a ME antenna involves performing structural analysis to determine the resonance mode required for the desired frequency. There are various classifications of piezoelectric resonators. Three commonly discussed types of thin-film resonators are those based on surface acoustic waves (SAWs),[24] bulk acoustic waves (BAWs),[25] and thin-film bulk acoustic wave resonators (FBARs).[26] SAWs primarily confine acoustic energy to the devices' surface but suffer from energy loss to the substrate. BAWs and FBARs have a high quality factor, but they typically operate in the thickness-excited S_1 mode in the GHz range above the medical implant communication service (MICS) band (402–405 MHz), since their resonant frequency is determined by the membrane thickness. Recently, a configuration called a laterally excited bulk wave resonator (XBAR)[27–31] has been implemented. This design utilizes Lamb waves that propagate in a thin film plate with periodic electrodes on top, similar to a SAW device. This design reduces the frequency dependence on the membrane thickness-to-wavelength ratio and provides more compatibility with complementary metal-oxide-semiconductor (CMOS) technology.[30] In the GHz region, XBARs demonstrate high phase velocity and strong piezoelectric coupling in the higher-order wave modes.[29,32]

In the MICS band, XBARs can carry more energy in A_0 mode and, thus, induce larger strain. Additionally, they do not require distributed reflectors to confine acoustic energy, as it is naturally confined by the piezo/air interface at the bottom surface of the membrane.

In this work, a 400 MHz XBAR ME antenna design is proposed. The resonator utilizes a heterostructure of magnetostrictive and piezoelectric membranes. Finite element method (FEM) simulation is carried out for both transmission and reception modes in the A_0 mode. Three models based on distinct physics are conducted in sequence, with results of one used as input for the next: piezoelectricity, micromagnetics, and magnetic dipole radiation. The decoupling has been empirically shown to sustain a satisfactory level of accuracy.[33] The radiation from the piezoelectric substrate and wires, considered as parasitic effects, are also considered. The strain-mediated switching process follows the equations below.

In a transmission mode, the piezoelectric thin film behavior under an applied voltage is first investigated. The model assumes linear piezoelectricity and electrostatics

$$\boldsymbol{\varepsilon} = s_E \boldsymbol{\sigma} + d^t \boldsymbol{E}, \tag{1}$$

$$\boldsymbol{D} = d\boldsymbol{\sigma} + \varepsilon_\sigma \boldsymbol{E}, \tag{2}$$

where $\boldsymbol{\varepsilon}$ is the strain, $\boldsymbol{\sigma}$ is the stress, $\boldsymbol{D}$ is the electric displacement, $\boldsymbol{E}$ is the electric field, d is the direct piezoelectric coupling matrix and the superscript t stands for its transposition, s_E is the compliance matrix under a constant electric field, and ε_σ is the permittivity under a constant stress field.

The piezoelectric strain induces a standing Lamb wave, which is an elastic wave that propagates in the piezoelectric thin film. It can be described using the sinusoidal solutions to these wave equations that satisfy the stress-free boundary conditions at top and bottom surfaces,[34]

$$\xi = A_x f_x(z) e^{i(\omega t - kx)}, \tag{3}$$

$$\zeta = A_z f_z(z) e^{i(\omega t - kx)}, \tag{4}$$

where ω is the angular frequency, and k is the wave number. The wavelength is $2\pi/k$ and the frequency is $\omega/2\pi$. The amplitude A and the displacement functions f depend on wave propagation direction x, plate thickness direction z, and time t only.

The piezoelectric strain is then transferred to the magnetoelastic layer, causing a reorientation of the magnetization. The precessional magnetization dynamics are governed by the Landau–Lifshitz–Gilbert (LLG) equation,

$$\frac{\partial \mathbf{m}}{\partial t} = -\mu_0 \gamma (\mathbf{m} \times \mathbf{H}_{\text{eff}}) + \alpha_G \left(\mathbf{m} \times \frac{\partial \mathbf{m}}{\partial t} \right), \tag{5}$$

where $\mathbf{m}$ is the normalized magnetization, μ_0 is the vacuum permittivity, γ is the gyromagnetic ratio, α_G is the Gilbert damping parameter, and $\mathbf{H}_{\text{eff}}$ is the effective magnetic field.

The reorientation of magnetization emits radiation as a magnetic dipole. The radial component of the induced magnetic field at a specific distance is expressed as follows:

$$H_r = j \frac{k m_0 \cos\theta}{2\pi r^2} \left(1 + \frac{1}{jkr} \right) e^{-jkr}, \tag{6}$$

where m_0 is the total magnetic dipole moment, r is the distance from the magnetic dipole.

In a reception mode, a sinusoidal magnetic field is imparted as an input, and the electromagnetic (EM) fields are initially computed in air and solid. The governing equation provided below is utilized, under the presumption that the resultant radiation from the magnetic material, the piezoelectric layer, and the transmission line is negligible,[33]

$$\nabla \times (\mu^{-1} \nabla \times \boldsymbol{A}) = -(j\omega\sigma - \omega^2 \varepsilon) A, \tag{7}$$

where $\boldsymbol{A}$ is the vector potential, σ is the conductivity, μ is the permittivity, and ε is the permittivity.

The magnetostriction of the magnetoelastic material under the applied field described above is given as follows:

$$\varepsilon_{me} = \frac{3}{2} \frac{\lambda_s}{M_s^2} dev(\boldsymbol{M} \otimes \boldsymbol{M}), \tag{8}$$

where λ_s is the saturation magnetostriction and M_s is the saturation magnetization. The operator dev is the derivative of magnetization tensor product. The calculated magnetostrictive strain induces deformation of the piezoelectric layer, which can then be converted into an output voltage signal based on the piezoelectric equations discussed above [Eqs. (1) and (2)]. The antenna design process is aided by the use of these models.

The XBAR ME antenna is a substrate-released structure consisting of a continuous 100-nm-thick Pt bottom electrode, a 1-μm-thick AlN piezoelectric layer, twenty 1-μm-thick Al top electrodes, and twenty 500-nm-thick FeGaB magnetic strips as shown in Fig. 1(a). The width of both the Al and FeGaB strips is 5.4 μm, which is a quarter wavelength at 400 MHz. The addition of a bottom electrode allows for an out-of-plane E-field to enhance the longitudinal wave (LW), providing stronger electromechanical coupling compared to classical interdigital transducers (IDTs) without the bottom electrode. This configuration also has less technological complexity compared to the IDT/over-floating configuration with a bottom electrode and both positive and negative top voltage ports. The use of etching vias at the central region of the device enables the removal of the underlying silicon substrate, resulting in the release of the membrane. This process eliminates mechanical substrate clamping and enhances the resonant strain produced in the AlN. The device works by applying out-of-plane E-field along the crystalline AlN c axis to produce a standing Lamb wave. This results in the lateral excitation of strain in both the AlN film and the FeGaB strips. The FeGaB strips' magnetization is, thus, reoriented and acts as a magnetic radiation source. Coherent magnetization switching is ensured by arranging of FeGaB strips between Al strips, maintaining in-phase strain relative to one another. The side view of the device is shown in Fig. 1(b). The strips width direction is defined as the x axis and the out-of-plane direction is defined as the z axis. The AlN film's x axis strain distribution upon applying voltage on top electrodes is shown in Fig. 1(c).

In transmission mode, a 3D finite element analysis (FEA) model in COMSOL Multiphysics is performed to predict the mechanical resonance response of the XBAR ME antenna. The analysis solves for electrostatics and solid mechanics only. The system includes the resonator, transmission line, and explicitly modeled etching vias and cavity geometries, as depicted in the inset of Fig. 2(b). The resonator is comprised of an AlN layer, bottom Pt electrode, top Al electrodes, and FeGaB magnetic strips, as previously described. The analysis also considers mechanical and dielectric loss. A constant input power of 1 mW

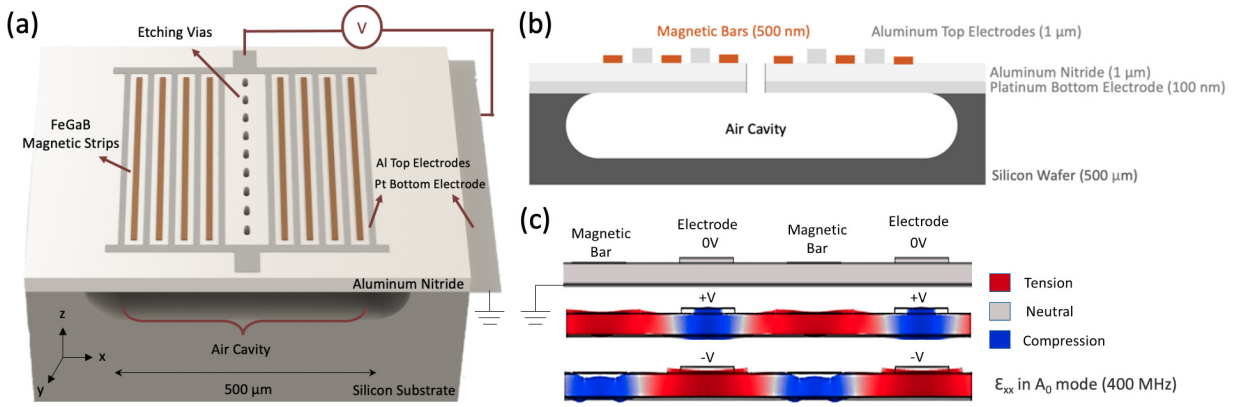

FIG. 1. (a) XBAR ME antenna diagram, not drawn to actual scale. (b) Cross-sectional view of device. (c) Strain distribution of A_0 mode Lamb wave.

is applied at one side of the Al transmission line via a terminal boundary condition, representing the input from the GSG probe. This results in the generation of a standing Lamb wave within the region covered by electrodes, which is absorbed by the perfectly matched layers at the sides and bottom.

Figure 2(a) depicts the simulated impedance curve that has been adjusted to match the experimentally measured impedance, using fitted parameters for Young's modulus, mechanical damping, and dielectric loss. A magnified representation of the A_0 mode shape is presented in the inset. It should be noted that the resonant frequency may deviate from the intended 400 MHz due to material properties and inconsistencies in microfabrication. The average strain in the FeGaB strips is also computed in the frequency domain. As illustrated in Fig. 2(b), the average strain in the strip width direction (x axis) prevails at resonance, corresponding to the LW propagation direction. The device as well as the fitted model exhibit a high quality factor of 500 compared to the conventional value of 100 for typical SAW structures.[35] The resulting strain is then utilized as the input for the subsequent micromagnetic simulation.

The strain at resonance is utilized in the micromagnetic model to determine the magnetization change. The Landau–Lifshitz–Gilbert (LLG) equation is employed to calculate the effective magnetic field, which encompasses the magnetoelastic field and other fields, including the demagnetization, Zeeman, and exchange field. The micromagnetic

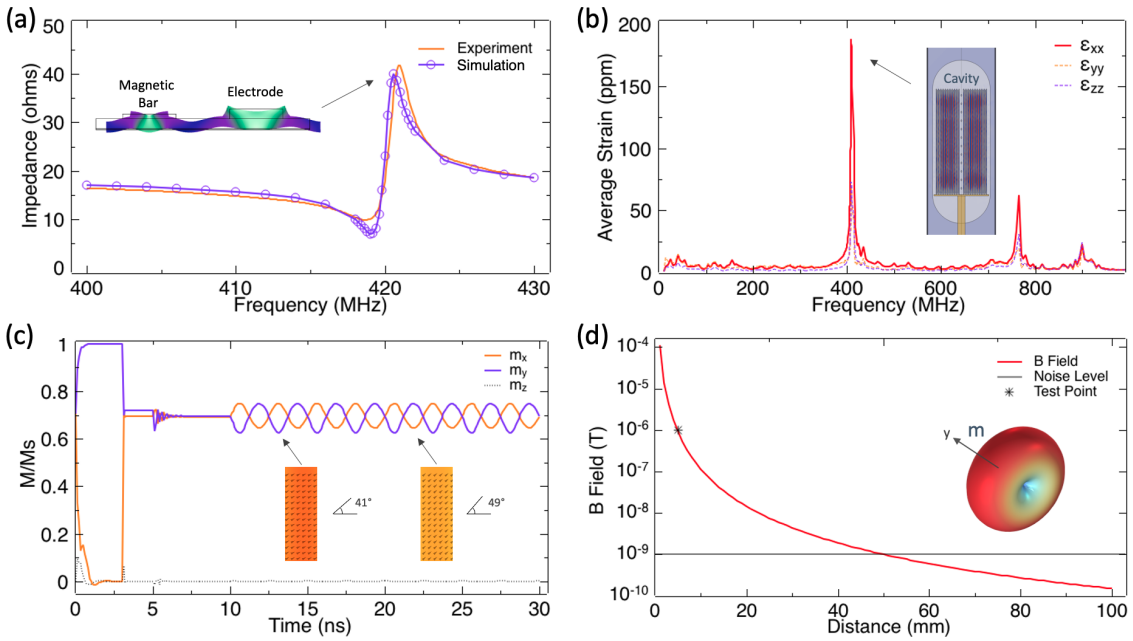

FIG. 2. (a) Simulated and measured impedance of the XBAR ME antenna, and the inset shows the A0 mode Lamb wave. (b) Simulated average strain in FeGaB strips, and the inset shows the strain distribution. (c) Simulated magnetization precession in time domain under applied AC voltage, and the inset shows the magnetization change. (d) Simulated induced magnetic field strength, and the inset shows the radiation pattern of a magnetic dipole.

model is essential as previous studies have reported that at high frequencies, the speed of sound-limited domain wall motion cannot keep pace with the dynamic strain's changing speed.[24] To optimize the computational efficiency, a $5.4 \times 5.4\,\mu m^2$ portion of a single $5.4 \times 1000\,\mu m$ magnetic strip is modeled, with periodic boundary conditions applied at the top and bottom to account for the shape anisotropy caused by the high aspect ratio of the strips. In the model, the magnetization is initially set in an arbitrary direction but rapidly reorients along the long axis (y axis) due to structure's shape anisotropy. A saturating bias magnetic field is then applied at 45° to align all magnetic domains, as 45° was determined to be the maximum coupling angle for efficient strain-magnetization interaction.[36] After all the domains are aligned, the bias field magnitude is reduced to half its strength to avoid pinning of the magnetization during device operation. The previously calculated dynamic strain is then applied along the x axis, resulting in magnetization oscillation. The results, depicted in Fig. 2(c), demonstrate a coherent 10% coherent magnetization rotation in each cycle, with the inset showing the different magnetization states in each cycle.

The magnetization change calculated from the micromagnetic model is utilized as the input in a FEM magnetic dipole model to predict the radiated magnetic field. The total magnetic moment can be determined by the FeGaB volume and the 10% magnetization rotation. The resulting radial component of the magnetic field is plotted against distance in Fig. 2(d), with the inset showing the radiation pattern for a magnetic dipole oriented along the y axis. The magnetic flux density signal strength exceeds 1 μT at a distance of 5 mm from the device under test (DUT) and falls below the 1 nT detectable limit at a distance of 5 cm, thus preventing information leakage in medical applications. It is worth noting that each structure, defined as a single antenna element, contains twenty FeGaB strips. It is important to note that the signal strength described above is generated by 100 elements functioning as an antenna array. The number of elements can be adjusted according to produce a detectable signal above the ambient noise threshold within a specified distance range.

The XBAR configuration lacks a continuous top metallic thin film, resulting in a diminished shielding effect against electric fields compared to the FBAR configuration. Consequently, the piezoelectric layer and wires in the device radiate as electric dipoles, which are considered parasitic as they do not produce the intended magnetic signal. To comprehensively evaluate the radiation, we use a FEM model to analyze the radiation pattern. Our model includes contributions from FeGaB strips as a magnetic dipole pointing along the y axis, the AlN layer as an electric dipole pointing along the z axis, and explicitly modeled wires. We separate and combine the contributions from each component of a single element and present the resulting field values in Table I. Our analysis indicates that the radiation from the magnetic dipole dominates in the near field, as shown in bold in the table.

In the reception mode, a reversed process is implemented in which a 2D FEM model is constructed to incorporate all relevant physical phenomena. This model is employed to simulate magnetostriction in FeGaB and the induced voltage in AlN, under the input of a spatially uniform, sinusoidal H field in the surrounding air. The constitutive equations are solved using a segregated approach. Specifically, Maxwell's equations are initially used to determine the global E and H fields, while neglecting radiation from the DUT. After that, the magnetoelastic strain in the FeGaB strips is calculated, followed by the induced voltage on Al electrodes by temporally assuming electrostatic conditions to solve for piezoelectricity in the solid.

To achieve an accurate reception mode model of the magnetization and magnetostriction of the device, the magnetic properties of FeGaB are experimentally measured. The results of the magnetic characterization of FeGaB using vibrating sample magnetometry (VSM) and beam bending magnetostriction are presented in Figs. 3(a) and 3(b). The data indicate that the material exhibits an easy axis with a low coercivity of 1 Oe and a high saturation magnetization of 1050 emu/cc. In addition, the saturation magnetostriction reaches 60 ppm, and the piezomagnetic coefficient is 4 ppm/Oe. Notably, the 400 MHz XBAR ME antenna operates in the linear region for both ferromagnetic and magnetoelastic materials.[37]

With these parameters, the simulated strain distribution at resonance in FeGaB strips and the out-of-plane E-field distribution in the AlN layer are shown in Fig. 3(c), demonstrating good agreement with the transmission mode model. Finally, Fig. 3(d) displays the induced ME voltage detected on the Al electrodes.

In order to validate the previously discussed modeling results, we fabricated a proof-of-concept antenna using traditional microfabrication techniques consisting of four distinct layers. The first layer is a 100-nm-thick Pt layer deposited on a 4-inch Si wafer, which serves as the bottom electrode. Then, a 1-μm-thick AlN film is then deposited as the piezoelectric material. Next, vias are wet-etched to expose the electrical ground contacts. Next, a 1-μm-thick Al layer is deposited and patterned as the top electrodes. After that, a 500-nm-thick FeGaB film with SiO_2 interlayers to prevent eddy currents is deposited and patterned as the magnetostrictive material. The deposition is performed with a in-plane bias magnetic field at 45° to align the magnetic domains and induce the easy axis for magnetization. Finally, the structure is released from the silicon substrate by a Cl_2-based inductively coupled plasma (ICP) etch, followed by a XeF_2 dry etch to chemically remove the Si beneath the antenna. The optical micrograph and zoomed-in picture of the device are shown in Fig. 4(a).

The S_{11} reflection coefficient of a single element is measured utilizing a 10 dBm input power applied to the GSG probe. The results, presented in Fig. 4(c), display a −13 dB mechanical resonance at 420 MHz. The deviation from the theoretical resonant frequency of 400 MHz can be attributed to variations in the microfabrication

TABLE I. Radiation of antenna components at 2 cm (V/m for electric field, A/m for magnetic field).

400 MHz	E (2,0,0)	H (2,0,0)	E (0,2,0)	H (0,2,0)	E (0,0,2)	H (0,0,2)
Al wires	3.1×10^{-4}	2.1×10^{-7}	3.4×10^{-4}	2.3×10^{-7}	7.3×10^{-4}	2.2×10^{-8}
FeGaB strips	7.3×10^{-3}	1.1×10^{-4}	2.6×10^{-5}	$\mathbf{2.3 \times 10^{-4}}$	7.3×10^{-3}	1.1×10^{-4}
AlN layer	4.0×10^{-4}	1.8×10^{-7}	3.8×10^{-4}	1.8×10^{-7}	8.1×10^{-4}	1.5×10^{-9}
Combined	3.8×10^{-2}	9.7×10^{-5}	4.8×10^{-2}	2.2×10^{-4}	3.3×10^{-2}	1.2×10^{-5}

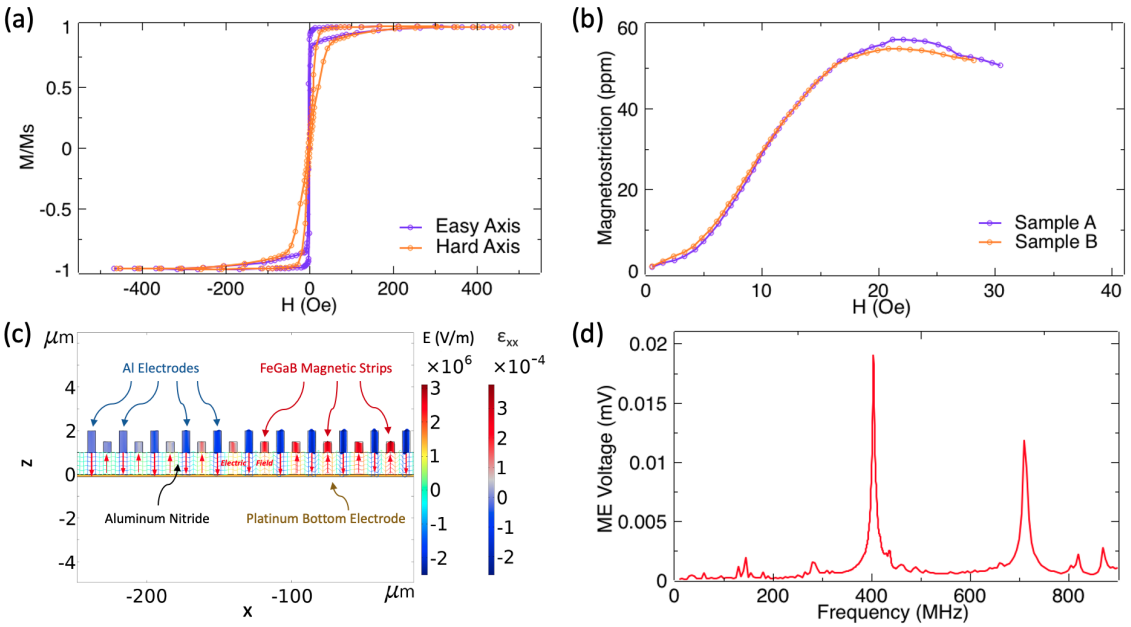

FIG. 3. (a) FeGaB magnetic hysteresis loop measured by VSM. (b) FeGaB magnetostriction curve measured by beam bending. (c) Simulated electric field distribution in AlN and strain distribution in Al electrodes and FeGaB strips. (d) Simulated induced voltage on Al top electrodes.

process. It is observed that the curve shifts in response to different DC magnetic bias fields by external magnets, which is a manifestation of the ΔE effect,[38] where the bias magnetic field modifies the Young's modulus of the FeGaB strips. These results demonstrate the device's ME coupling and the resonance frequency's tunability.

The transmission coefficient S_{21} of a single element is measured utilizing a probe station. The input power of 30 dBm is applied to port one after amplification, which is connected to the GSG pad. Port two was connected to a magnetic probe positioned on top of the device at approximately 5 mm. The experimental setup is depicted in Fig. 4(b).

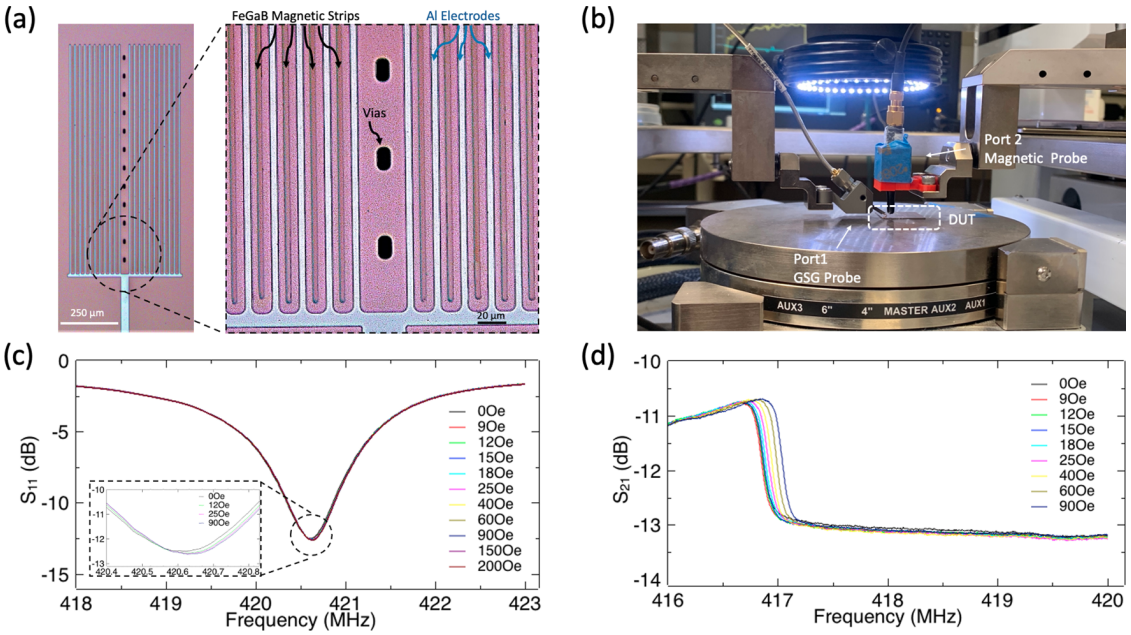

FIG. 4. (a) Optical micrograph of the device. (b) Image of the test setup with the XBAR ME antenna transmitting and the log antenna receiving. (c) Measured S11 of the device at various bias magnetic fields. (d) Measured S21 of the device at various bias magnetic fields.

As shown in Fig. 4(d), the detected magnetic field strength reaches its maximum at the resonance frequency. The results also indicate a shift in the S_{21} curve under varying bias DC magnetic fields, which again can be attributed to the ΔE effect. This demonstrates the device's ability to radiate detectable magnetic signals with tunability. Efforts in previous studies have aimed to eliminate parasitic effects and isolate the magnetic signal.[7,12,26,33] However, such efforts are beyond the scope of this investigation.

In conclusion, we present a 400 MHz XBAR ME antenna that operates at acoustic resonance for use in implantable device communication systems. The size of the element, $400 \times 1000\ \mu m^2$, is orders of magnitude smaller than conventional antennas. In the transmission mode, we analyze three aspects of the FEM simulation: piezoelectricity, micromagnetics, and magnetic dipole radiation, while considering parasitic effects from the piezoelectric substrate and wire. In reception mode, we employ an integrated FEM model with a segregated solver to investigate the device's behavior. The final fabricated device demonstrates mechanical resonance with a Q-factor of 500 and ME coupling through S_{11} and S_{21} measurements. The device displays promise for compact antenna design and the possibility of array arrangements to maximize radiated power.

The authors would like to thank Schaffer Grimm, M. K. Panduranga, Ting Lu, and Sidhant Tiwari for their valuable discussions and microfabrication support. This work was partially supported by NSF Nanosystems Engineering Research Center for Translational Applications of Nanoscale Multiferroic Systems (TANMS) Cooperative Agreement Award No. EEC-1160504.

AUTHOR DECLARATIONS

Conflict of Interest

The authors have no conflicts to disclose.

Author Contributions

Ruoda Zheng and Victor Estrada contributed equally to this work.

Ruoda Zheng: Conceptualization (lead); Software (equal); Writing – original draft (equal). **Rashaunda Henderson:** Conceptualization (supporting); Resources (supporting); Validation (equal). **Gregory P. Carman:** Conceptualization (equal); Resources (equal); Supervision (equal). **Abdon E. Sepulveda:** Conceptualization (equal); Resources (equal); Supervision (lead). **Victor Estrada:** Conceptualization (equal); Investigation (equal); Writing – review & editing (equal). **Nishanth Virushabadoss:** Data curation (lead); Validation (lead). **Alexandria Will-Cole:** Resources (equal). **Adrian Acosta:** Resources (equal). **Jinzhao Hu:** Conceptualization (supporting). **Wenzhong Yan:** Resources (supporting). **Jane P. Chang:** Resources (supporting). **Nian-Xiang Sun:** Resources (supporting).

DATA AVAILABILITY

Raw data were generated at the Department of Mechanical and Aerospace Engineering, University of California, Los Angeles, and the Department of Electrical and Computer Engineering, University of Texas at Dallas. The data that support the findings of this study are available from the corresponding author upon reasonable request.

REFERENCES

[1]A. Erentok and R. W. Ziolkowski, Microw. Opt. Technol. Lett. **49**(6), 1287–1290 (2007).
[2]S. Lim and H. Ling, Electron. Lett. **42**(16), 895–897 (2006).
[3]R. W. Ziolkowski, IEEE Antennas Wirel. Propag. Lett. **7**, 217 (2008).
[4]F. Rangriz, A. Khaleghi, and I. Balasingham, in *14th European Conference on Antennas and Propagation (EuCAP)* (IEEE, 2020).
[5]M. A. Kemp, M. Franzi, A. Haase, E. Jongewaard, M. T. Whittaker, M. Kirkpatrick, and R. Sparr, Nat. Commun. **10**(1), 1–7 (2019).
[6]J. Xu, C. M. Leung, X. Zhuang, J. Li, S. Bhardwaj, J. Volakis, and D. Viehland, Sensors (Switzerland) **19**, 853 (2019).
[7]J. D. Schneider, J. P. Domann, M. K. Panduranga, S. Tiwari, P. Shirazi, Z. Yao, C. Sennott, D. Shahan, S. Selvin, G. McKnight, W. Wall, R. N. Candler, Y. E. Wang, and G. P. Carman, J. Appl. Phys. **126**(22), 224104 (2019).
[8]J. A. Bickford, R. S. Mcnabb, P. A. Ward, D. K. Freeman, and M. S. Weinberg, in *IEEE International Symposium on Antennas and Propagation & USNC/URSI National Radio Science Meeting* (IEEE, 2017), p. 1475.
[9]M. N. Srinivas Prasad, F. Fereidoony, and Y. E. Wang, in *IEEE International Symposium on Antennas and Propagation and North American Radio Science Meeting* (IEEE, 2020), p. 1305.
[10]Z. Yao, Y. E. Wang, S. Keller, and G. P. Carman, IEEE Trans. Antennas Propagat. **63**, 3335 (2015).
[11]Z. Chu, C. Dong, C. Tu, X. Liang, H. Chen, C. Sun, Z. Yu, S. Dong, and N. X. Sun, Appl. Phys. Lett. **115**, 162901 (2019).
[12]C. Dong, X. Wang, H. Lin, Y. Gao, N. X. Sun, Y. He, M. Li, C. Tu, Z. Chu, X. Liang, H. Chen, Y. Wei, and M. Zaeimbashi, IEEE Antennas Wirel. Propag. Lett. **19**, 398 (2020).
[13]A. E. Hassanien, M. Breen, M. H. Li, and S. Gong, Sci. Rep. **10**(1), 1–12 (2020).
[14]H. Lin, M. Zaeimbashi, N. N. X. N. Sun, X. Liang, H. Chen, C. Dong, A. Matyushov, X. Wang, Y. Guo, Y. Gao, and N. N. X. N. Sun, in *IEEE MTT-S International Microwave Symposium Digest* (IEEE, 2018), p. 220.
[15]P. J. Shah, D. A. Bas, I. Lisenkov, A. Matyushov, N. X. Sun, and M. R. Page, Sci. Adv. **6**, eabc5648 (2020).
[16]H. Chen, C. Dong, Y. Wei, J. G. Jones, M. E. McConney, M. R. Page, B. M. Howe, G. J. Brown, N. N. X. Sun, X. Wang, Y. Gao, X. Shi, Z. Wang, N. N. X. Sun, M. Zaeimbashi, X. Liang, and Y. He, IEEE Trans. Microwave Theory Tech. **68**, 951 (2020).
[17]M. Nasrollahpour, A. Romano, M. Zaeimbashi, X. Liang, H. Chen, N. N. X. Sun, S. Emam, M. Onabajo, and N. N. X. Sun, Analog Integr. Circ. Sig. Process. **105**, 407 (2020).
[18]X. Liang, H. Chen, and N. X. Sun, APL Mater. **9**, 041114 (2021).
[19]C. Tu, Z. Q. Chu, B. Spetzler, P. Hayes, C. Z. Dong, X. F. Liang, H. H. Chen, Y. F. He, Y. Y. Wei, I. Lisenkov, H. Lin, Y. H. Lin, J. McCord, F. Faupel, E. Quandt, and N. X. Sun, Materials (Basel) **12**, 2259 (2019).
[20]M. Zaeimbashi, H. Lin, C. Dong, X. Liang, M. Nasrollahpour, H. Chen, N. N. N. Sun, A. Matyushov, Y. He, X. Wang, C. Tu, Y. Wei, Y. Zhang, S. S. Cash, M. Onabajo, A. Shrivastava, and N. N. N. Sun, IEEE J. Electromagn. RF Microwave Med. Biol. **3**, 206 (2019).
[21]J. Lou, R. E. Insignares, Z. Cai, K. S. Ziemer, M. Liu, and N. X. Sun, Appl. Phys. Lett. **91**, 182504 (2007).
[22]M. Zaeimbashi, M. Nasrollahpour, A. Khalifa, A. Romano, X. Liang, H. Chen, N. Sun, A. Matyushov, H. Lin, C. Dong, Z. Xu, A. Mittal, I. Martos-Repath, G. Jha, N. Mirchandani, D. Das, M. Onabajo, A. Shrivastava, S. Cash, and N. X. Sun, Nat. Commun. **12**, 1–11 (2021).
[23]M. Li, A. Matyushov, C. Dong, H. Chen, H. Lin, T. Nan, Z. Qian, M. Rinaldi, Y. Lin, and N. X. Sun, Appl. Phys. Lett. **110**, 143510 (2017).
[24]J. L. Drobitch, A. De, K. Dutta, P. K. Pal, A. Adhikari, A. Barman, and S. Bandyopadhyay, Adv. Mater. Technol. **5**, 2000316 (2020).
[25]Z. Yao, S. Tiwari, T. Lu, J. Rivera, K. Q. T. Luong, R. N. Candler, G. P. Carman, and Y. E. Wang, IEEE J. Multiscale Multiphys. Comput. Tech. **5**, 5 (2020).
[26]T. Nan, H. Lin, Y. Gao, A. Matyushov, G. Yu, H. Chen, N. N. X. N. Sun, S. Wei, Z. Wang, M. Li, X. Wang, A. Belkessam, R. Guo, B. Chen, J. Zhou, Z. Qian, Y. Hui, M. Rinaldi, M. E. McConney, B. M. Howe, Z. Hu, J. G. Jones, G. J. Brown, and N. N. X. N. Sun, Nat. Commun. **8**(1), 1–8 (2017).
[27]L. Arapan, I. Katardjiev, and V. Yantchev, J. Micromech. Microeng. **22**(8), 085004 (2012).

[28]Y. Liu, Y. Cai, Y. Zhang, A. Tovstopyat, S. Liu, and C. Sun, Micromachines **11**, 630 (2020).
[29]S. Yandrapalli, V. Plessky, J. Koskela, V. Yantchev, P. Turner, and L. G. Villanueva, in *IEEE International Ultrasonics Symposium* (IEEE, 2019), p. 185.
[30]V. Yantchev and I. Katardjiev, J. Micromech. Microeng. **23**(9), 095002 (2013).
[31]J. D. Schneider, T. Lu, S. Tiwari, X. Zou, A. Mal, R. N. Candler, Y. E. Wang, and G. P. Carman, J. Appl. Phys. **128**(6), 64105 (2020).
[32]A. R. Will-Cole, A. E. Hassanien, S. D. Calisgan, M. G. Jeong, X. Liang, S. Kang, V. Rajaram, I. Martos-Repath, H. Chen, A. Risso, Z. Qian, S. M. Seyed Abrishami, N. Lobandi, M. Rinaldi, S. Gong, and N. X. Sun, J. Appl. Phys. **131**(24), 241101 (2022).
[33]Z. Zhou, S. Keller, A. Sepulveda, and G. Carman, IEEE J. Multiscale Multiphys. Comput. Tech. **1**, 129 (2016).
[34]C. Willberg, S. Duczek, J. M. Vivar Perez, D. Schmicker, and U. Gabbert, Comput. Methods Appl. Mech. Eng. **241–244**, 246 (2012).
[35]Y. K. Yong, M. Patel, J. Vig, and A. Ballato, IEEE Trans. Ultrason. Ferroelectr. Freq. Control **56**, 353 (2009).
[36]D. Labanowski, A. Jung, and S. Salahuddin, Appl. Phys. Lett. **108**, 022905 (2016).
[37]C. Dong, M. Li, X. Liang, H. Chen, H. Zhou, X. Wang, Y. Gao, M. E. McConney, J. G. Jones, G. J. Brown, B. M. Howe, and N. X. Sun, Appl. Phys. Lett. **113**, 262401 (2018).
[38]T. Nan, Y. Hui, M. Rinaldi, and N. X. Sun, Sci. Rep. **3**, 1985 (2013).